Journal of Materials Chemistry A

Accepted Manuscript

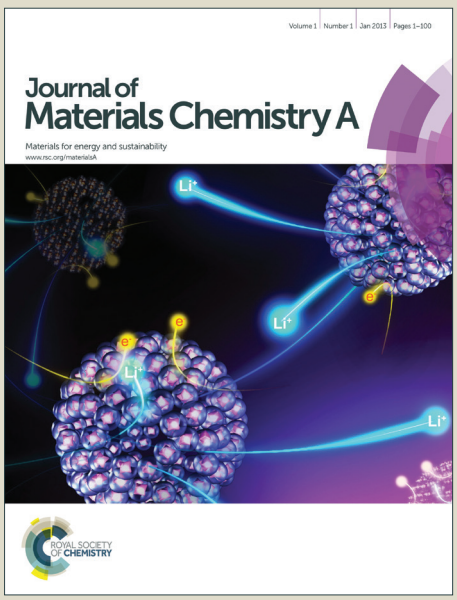

ROYAL SOCIETY OF CHEMISTRY

www.rsc.org/materialsA

Table of Contents

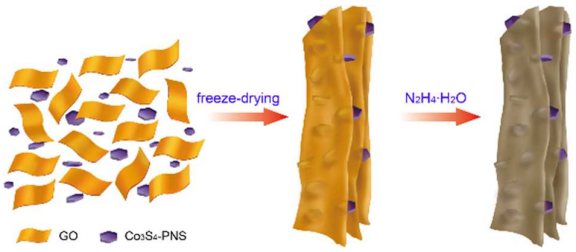

A robust three-dimensional sandwich-like Co_3S_4 porous nanosheets/graphene sheets composite exhibits improved rate performance and cycling stability for both lithium and sodium storage.

Journal Name

RSCPublishing

COMMUNICATION

Co_3S_4 porous nanosheets embedded in graphene sheets as high-performance anode materials for lithium and sodium storage

Cite this: DOI: 10.1039/x0xx00000x

Received 00th January 2012,
Accepted 00th January 2012

DOI: 10.1039/x0xx00000x

www.rsc.org/

Yichen Du,[a] Xiaoshu Zhu,[b] Xiaosi Zhou,*[,a] Lingyun Hu,[a] Zhihui Dai,[a] and Jianchun Bao*[,a]

Co_3S_4 porous nanosheets embedded in flexible graphene sheets has been synthesized through a simple freeze-drying and subsequent hydrazine treatment process. The robust structural stability of the as-prepared three-dimensional sandwich-like Co_3S_4-PNS/GS composite affords improved rate performance and cycling stability for both lithium and sodium storage.

As one of the most effective energy-storage devices, rechargeable lithium-ion batteries (LIBs) have attracted much attention due to their advantages including high energy and power density and environmental benignity.[1–8] Graphite, the traditional anode material for the current LIBs, has become one of the limiting factors for obtaining high energy density batteries because of its low theoretical capacity of 372 mA h g^{-1}.[9] In order to meet the growing energy demand, tremendous effort has been devoted to designing and synthesizing novel anode materials with higher theoretical capacity, such as Li-alloying materials (Sn, Sb, Ge, and Si)[10–19] and transition metal dichalcogenides (TMD).[20–30] However, all these materials suffer from huge volume changes during Li insertion and extraction, which causes serious pulverization of the electrodes and thus rapid capacity decay. For example, Si possesses a high specific capacity of 4200 mA h g^{-1} for $Li_{4.4}Si$, however, it undergoes extreme large volume variation (~400%) during cycling. Such huge volume changes result in significant mechanical stress of the electrode and thereby lower the cycle life of the Si anode.[31,32] Despite many strategies have been proposed to improve the electrochemical capability of Si-based anodes including fabricating Si nanostructures and synthesizing Si/carbon nanocomposites,[33–35] it remains challenging to overcome the drawback of inherent volume expansion of these materials upon cycling.

The development of new electrode materials is urgent to construct next-generation of LIBs with high energy and power densities to satisfy the future demand for electronic vehicles and large-scale storage of renewable energy. Cobalt sulfides have been extensively investigated as promising anode materials for LIBs due to its high theoretical capacity.[36–43] However, the low electrical conductivity and ionic diffusion in their bulk forms generally result in limited lithium storage properties.[44–46] Let alone the larger radius of Na^+, it will lead to even worse electrochemical performance when sodium storage is concerned. It has been reported that nanosized cobalt sulfide particles could significantly enhance the lithium ion diffusion.[47] Unfortunately, severe agglomeration of nanoparticles during the lithium uptake and release processes limits the applicability of this strategy. Recently, it has been proposed that combining cobalt sulfide porous structures with highly conductive graphene could partially address this issue while exhibiting good electrochemical performance.[48,49] However, the reported cobalt sulfide/graphene composites demonstrate less satisfactory long-term cycling stability, which perhaps originates from the poor structural stability of these composites.

Herein, we report a facile and cost-effective approach to design and prepare Co_3S_4 porous nanosheets/graphene sheets (denoted as Co_3S_4-PNS/GS) composite with unique sandwich-like architecture through freeze-drying and subsequent hydrazine treatment. The as-prepared composite benefits from the synergistic effect of its two components. Specifically, the encapsulated Co_3S_4 porous nanosheets effectively facilitate ion transport and accommodate the volume expansion. Besides, the excellent electrical and mechanical properties of graphene sheets can not only improve the electrode conductivity but also well buffer the large volume changes of Co_3S_4 during cycling. As a result, Co_3S_4-PNS/GS composite manifests enhanced cycling stability and rate performance compared with that of Co_3S_4-PNS.

As illustrated in Scheme 1, the preparation of Co_3S_4-PNS/GS composite is straightforward and simple. Graphene oxide (GO) obtained by a modified Hummer's method were well dispersed into deionized water via sonication,[50] followed by the addition of Co_3S_4-PNS aqueous suspension. Next, the mixture was immediately frozen by using liquid nitrogen and subsequent freeze-dried in order to achieve a firm and conformal GO coating on the surface of Co_3S_4-PNS. A sandwich-type Co_3S_4-PNS/GO precursor was generated after the freeze-drying process, the formation of which was assisted by the van der Waals interaction between Co_3S_4-PNS and GO. Finally, the composite Co_3S_4-PNS/GS consisting of porous Co_3S_4 nanosheets and graphene

sheets could be obtained after a simple hydrazine treatment, in which Co_3S_4-PNS is embedded into the galleries of graphene sheets due to $\pi-\pi$ interaction between graphene sheets.[28] The detailed procedure is described in Experimental Section in the Supporting Information.

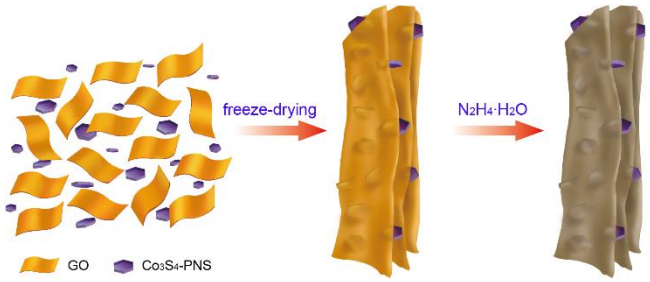

Scheme 1. Schematic illustration of the formation of sandwich-type Co_3S_4-PNS/GS composite.

To survey the phase structure and surface composition of the Co_3S_4-PNS/GS composite, X-ray diffraction (XRD) and X-ray photoelectron spectroscopy (XPS) analyses were carried out. The XRD pattern (Figure 1a) shows that the diffraction peaks can be readily indexed to cubic Co_3S_4 phase (JCPDS card No. 47-1738). The broadened diffraction peaks imply that the Co_3S_4 porous nanosheets in the composite are composed of small nanocrystals. In addition, five elements including Co, S, C, O, and N are detected in the XPS survey scan of the Co_3S_4-PNS/GS composite from 0 to1100 eV (Fig. S1†). Their respective atomic percentage is 2.68%, 3.80%, 70.67%, 17.42%, and 5.43%. The atomic ratio of S to Co is approximately 1.42, closed to the theoretical value for Co_3S_4. The high-resolution Co 2p XPS spectrum of the composite displays peaks at 797.1 and 781.8 eV, which are related to the Co $2p_{1/2}$ and Co $2p_{3/2}$ characteristic peaks of Co_3S_4-PNS, respectively (Figure 1b). As to the peaks at 794.0 and 778.8 eV, we ascribe them to the Co–O bond, suggesting partial surface oxidation. Meanwhile, two broad peaks observed at 802.4 and 786.4 eV can be attributed to the satellite peaks of Co 2p, which are in good agreement with the reported values.[51] The existence of Co_3S_4-PNS can be further verified by the two evident S 2p peaks at 163.1 eV (S $2p_{1/2}$) and 161.9 eV (S $2p_{3/2}$) (Figure 1c). C 1s (284.8 eV) and O 1s (531.9 eV) peaks are commonly ascribed to the carbon and oxygen atoms in GS. The deconvolution of the C 1s peak is demonstrated in Figure 1d. Peaks located at 285.7, 286.5, 287.8, and 289.1 eV correspond to the carbon atoms in C=N, C–O, C=O, and O-C=O groups, respectively. Compared with the fitting results of GO,[21] the peak intensities of oxygen-containing functional groups reduce dramatically, suggesting the restoration of sp^2 hybridized graphene structure. Additionally, an obvious peak centered at 400.0 eV (Fig. S1†) indicates the formation of N-doped graphene sheets, which can enhance the lithium storage properties of composites through improving the electric conductivity of the carbon matrix.[11] Furthermore, the Co_3S_4 content in the Co_3S_4-PNS/GS composite measured by thermogravimetric analysis (TGA, Fig. S2†) is about 70.8 wt %. The porous feature of Co_3S_4-PNS/GS is examined by nitrogen adsorption–desorption analysis. As displayed in Fig. S3†, the nitrogen adsorption–desorption isotherms shows a typical IV-type isotherm with an associated H3 type hysteresis loop, suggesting a mesoporous characteristic of the composite. The pore size distribution (inset of Fig. S3†) calculated by the Barrett–Joyner–Halenda (BJH) method confirms the presence of mesopores of 2–10 nm in size. Besides, such a composite shows a low Brunauer–Emmett–Teller (BET) specific surface area of 16.8 $m^2\ g^{-1}$, indicating that the Co_3S_4-PNS are well wrapped by GS.

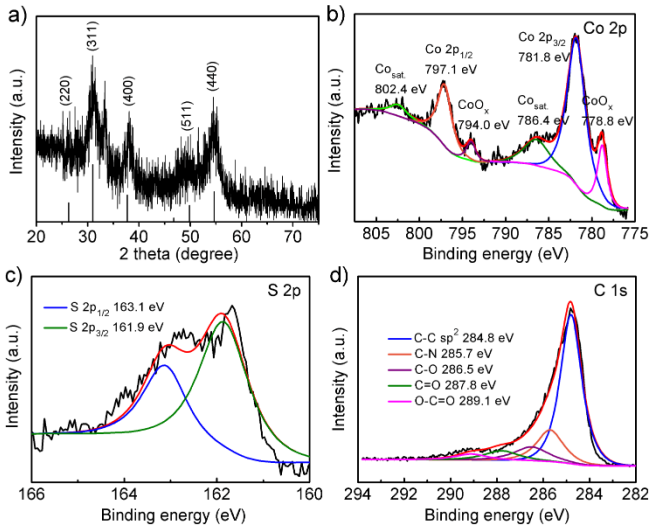

Fig. 1. (a) XRD pattern of Co_3S_4-PNS/GS and standard XRD pattern of Co_3S_4 (JCPDS card No. 47-1738). High-resolution XPS spectra of Co_3S_4-PNS/GS: (b) Co 2p, (c) S 2p, and (d) C 1s.

The morphology and structure of Co_3S_4-PNS and Co_3S_4-PNS/GS were analyzed by scanning electron microscopy (SEM) and transmission electron microscopy (TEM). Both SEM (Figure 2a) and TEM (Figure 2b) images of Co_3S_4 show hexagonal and porous sheet-like nanostructure with a lateral length of about 220 nm and a vertical height of around 30 nm. From the SEM image of Co_3S_4-PNS/GS (Figure 2c), we can observe that wrinkled GS intimately coat around Co_3S_4-PNS because of its flexibility. The TEM image (Figure 2d) of the Co_3S_4-PNS/GS composite clearly reveals a three-dimensional (3D) sandwich-type architecture that porous Co_3S_4 nanosheets are uniformly distributed between the interlayer galleries of GS. The high-resolution TEM (HRTEM) image (Figure 2e) and selected-area electron diffraction (SAED) pattern (inset of Figure 2e) display that the Co_3S_4 sample in the as-prepared Co_3S_4-PNS/GS is porous polycrystalline composed of highly crystalline nanoparticles. Based on the HRTEM image, there are about nine layers of GS wrapping around the edges of Co_3S_4-PNS, which have an interplanar distance of approximately 0.28 nm, corresponding to the (311) crystal plane of cubic Co_3S_4. Moreover, the scanning transmission electron microscopy (STEM) image (Figure 2f) and energy-dispersive X-ray spectroscopy (EDX) elemental mappings (Figure 2g–j) of the as-obtained composite show that Co_3S_4-PNS are homogeneously embedded in GS. The above results suggest the good combination of porous Co_3S_4 nanosheets and flexible graphene sheets, which can effectively accommodate the tremendous volume changes of Co_3S_4 during repeated Li or Na insertion/extraction processes, implying that the Co_3S_4-PNS/GS composite holds good mechanical integrity. The high robustness of the composite has been further confirmed by sonicating the sample for 30 minutes. From SEM and TEM images (Figure 2c and 2d), no obvious crack or collapse can be observed for the composite. This outstanding structural stability would be beneficial to reversible lithium and sodium storage with prolonged cycle life.

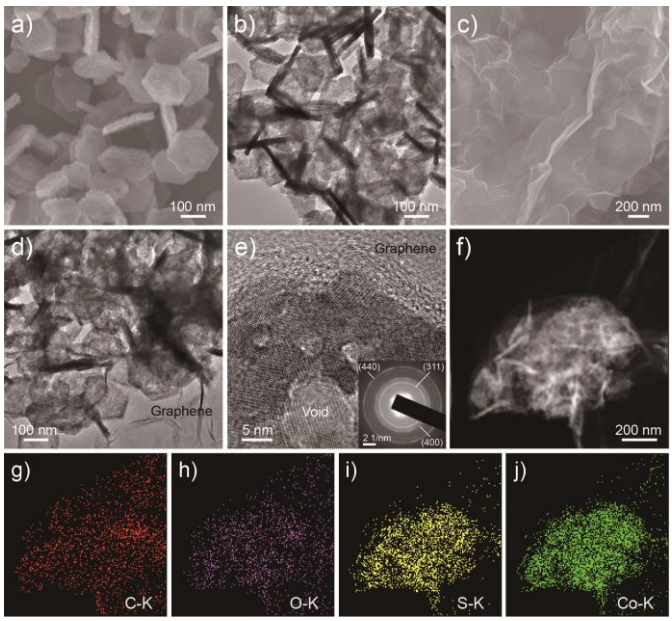

Fig. 2. (a, b) SEM and TEM images of Co_3S_4-PNS. (c) SEM image, (d) TEM image, (e) HRTEM image and SAED pattern (inset), (f) STIM image, and (g–j) EDX elemental mapping images of Co_3S_4 porous nanosheets embedded in graphene sheets (Co_3S_4-PNS/GS).

To illustrate the advantages of the robust Co_3S_4-PNS/GS, we investigated its lithium storage properties. The cyclic voltammograms (Fig. S4†) display the characteristic Li insertion/extraction behaviors for Co_3S_4. Figure 3a shows the discharge/charge profiles for different cycles at a current density of 0.5 A g^{-1} in the voltage range of 0.005−3 V vs Li^+/Li. The initial discharge and charge capacities are 1210 and 816 mA h g^{-1}, respectively, corresponding to a Coulombic efficiency of 67.4%. The capacity loss is mainly attributed to the formation of a gel-like polymeric layer (solid electrolyte interphase, SEI) and the irreversible conversion reaction between Li and Co_3S_4. Note that all the capacity values in this work are calculated based on the total mass of the composite. The Coulombic efficiency exceeds 96% at the 3rd cycle, and further increases to 99% after 6 cycles. As displayed in Figure 3b, Co_3S_4-PNS/GS shows excellent rate performance at discharge−charge current densities from 0.5 to 20 A g^{-1}. The average charge capacities are 726, 655, 602, 504, 405, and 295 mA h g^{-1} at current densities of 0.5, 1, 2, 5, 10, and 20 A g^{-1}, respectively. After the high rate cycling, the charge capacity can restore to 669 mA h g^{-1} when the current density is finally decreased to 0.5 A g^{-1}. Moreover, the composite exhibits superior cycling stability at a current density of 0.5 A g^{-1} (Figure 3c). The capacity decays from 816 to 672 mA h g^{-1} in the initial 20 cycles and keeps quite stable up to 200 cycles. Both long-term cycling stability and specific capacity of Co_3S_4-PNS/GS are better than those of pure Co_3S_4-PNS or GS under the same testing conditions (Fig. S5†). It is worth mentioning that the large irreversible capacity of Co_3S_4-PNS is due to the substantial volume changes of Co_3S_4-PNS during cycling, which cause the pulverization and subsequent inactivation of Co_3S_4-PNS. After 200 cycles, the capacities of Co_3S_4-PNS and GS significantly decrease to 37 and 259 mA h g^{-1}, respectively, while the composite exhibits a charge capacity of 710 mA h g^{-1}. Clearly, the electrochemical difference between Co_3S_4-PNS/GS and Co_3S_4-PNS indicates that the 3D sandwich-like structure can remarkably improve electronic and ionic transport throughout the electrode, which result in enhanced electrochemical kinetics. This is further proved by the EIS results (Fig. S6†), that is, the charge-transfer resistance value of Co_3S_4-PNS/GS (19.0 Ω) is much lower than that of Co_3S_4-PNS (45.9 Ω).

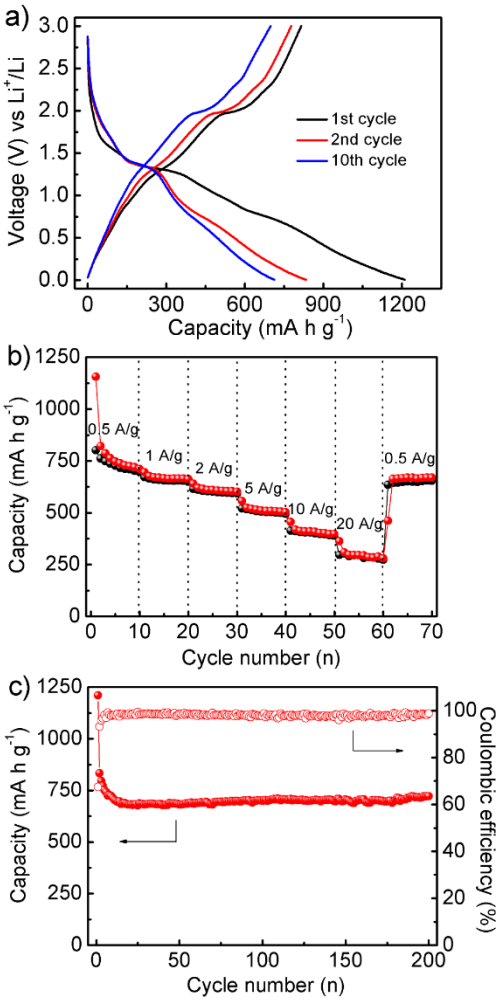

Fig. 3. Electrochemical performance of Co_3S_4-PNS/GS for lithium storage. (a) Galvanostatic discharge−charge profiles for different cycles at a current density of 0.5 A g^{-1}. (b) Rate capability at various current densities from 0.5 to 20 A g^{-1}. (c) Cycling performance and corresponding Coulombic efficiency at 0.5 A g^{-1}.

Additionally, we evaluated the sodium storage behavior of the Co_3S_4-PNS/GS composite (Figure 4). To our knowledge, there is no report available in the literature until now. The charge−discharge profiles (Figure 4a) are similar to those for lithium storage, only with lower voltage plateaus and capacities, which are due to the difference in energy barriers for the insertion and extraction of lithium and sodium ions. Due to the larger ionic radius of Na^+ than Li^+, the kinetics of sodium insertion and extraction are more sluggish compared to lithium.[23] The Coulombic efficiency of the first cycle is 53% and exceeds 96% after the 6th cycle. The rate performance is shown in Figure 4b. The average charge capacities are 423, 353, 307, 237, and 154 mA h g^{-1} at current densities of 0.5, 1, 2, 5, and 10 A g^{-1}, respectively. Likewise, the excellent rate performance can be ascribed to the 3D sandwich-type structure Co_3S_4-PNS/GS. The

cycling performance for sodium storage is good as well. After 50 cycles, a charge capacity of 329 mA h g^{-1} and more than 71% capacity retention are achieved at a current density of 0.5 A g^{-1} (Figure 4c). Besides, SEM and TEM images of the electrode material Co_3S_4-PNS/GS after cycling test shows that the 3D sandwich-like structure is almost maintained (Fig. S7†), indicating the excellent structural robustness of Co_3S_4-PNS/GS.

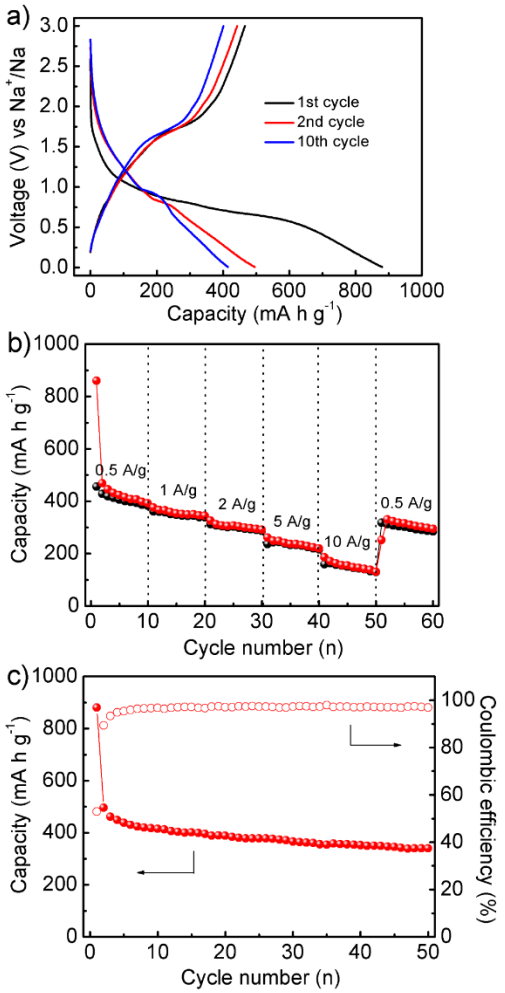

Fig. 4. Electrochemical performance of Co_3S_4-PNS/GS for sodium storage. (a) Galvanostatic discharge−charge profiles for different cycles at a current density of 0.5 A g^{-1} in the voltage range of 0.005−3 V vs Na^+/Na. (b) Rate capability at various current densities from 0.5 to 10 A g^{-1}. (c) Cycling performance and corresponding Coulombic efficiency at 0.5 A g^{-1}.

The outstanding rate performance and cycling stability of the as-synthesized Co_3S_4-PNS/GS composite as anode materials for both lithium and sodium storage can be understood from the following aspects. First, the small size of the primary Co_3S_4 nanocrystals and relatively thin GS coating shorten the diffusion distance for ions, thus realizing fast and reversible Li^+ or Na^+ insertion/extraction. Second, both the flexible graphene coating and the sub-micrometer size of the Co_3S_4 porous nanosheets smartly avoids the common aggregation of conventional nanoparticles. Third, the 3D sandwich-like architecture composed of porous Co_3S_4 nanosheets and high conductive graphene sheets not only provides pores and channels for rapid ion and electron transport but also effectively accommodates the large volume expansion, which guarantees the integrity of the electrode and enhances the capacity retention during repeated charge−discharge cycling. These unique nanostructures would improve the lithium and sodium storage properties and result in high specific capacity particularly at high rates.

Conclusions

In summary, a Co_3S_4-PNS/GS composite consisting of Co_3S_4 porous nanosheets and graphene sheets has been fabricated through a simple freeze-drying and subsequent hydrazine treatment approach. Due to the robust 3D sandwich-type architecture and porous nanostructure, the Co_3S_4-PNS/GS composite exhibits improved electrochemical performance. For lithium storage, the specific capacity is 710 mA h g^{-1} even after 200 cycles at a current density of 0.5 A g^{-1}. For sodium storage, a charge capacity of 329 mA h g^{-1} and more than 71% capacity retention are obtained after 50 cycles at 0.5 A g^{-1}, and the charge capacities are 237 and 154 mA h g^{-1} at 5 and 10 A g^{-1}, respectively. This work is expected to be favorable for the exploitation of high-performance Co_3O_4-based anodes for lithium and sodium storage.

Acknowledgements

This work was supported by the National Natural Science Foundation of China (Grant Nos. 21171096 and 21175069), the Natural Science Foundation of Jiangsu Province of China (BK20140915), the Scientific Research Foundation for Advanced Talents of Nanjing Normal University (2014103XGQ0073), the financial support from the Priority Academic Program Development of Jiangsu Higher Education Institutions, and the Program of Jiangsu Collaborative Innovation Center of Biomedical Functional Materials.

Notes and references

[a] Jiangsu Key Laboratory of Biofunctional Materials, School of Chemistry and Materials Science, Nanjing Normal University, Nanjing 210023, P. R. China. E-mail: zhouxiaosi@njnu.edu.cn; baojianchun@njnu.edu.cn
[b] Center for Analysis and Testing, Nanjing Normal University, Nanjing 210023, P. R. China

† Electronic Supplementary Information (ESI) available: Experimentional details, additional data on Co_3S_4-PNS/GS, Co_3S_4-PNS, and GS. See DOI: 10.1039/c000000x/

1 M. Armand and J.-M. Tarascon, *Nature*, 2008, **451**, 652.
2 K. Kang, Y. S. Meng, J. Bréger, C. P. Grey and G. Ceder, *Science*, 2006, **311**, 977.
3 J. B. Goodenough and Y. Kim, *Chem. Mater.*, 2010, **22**, 587.
4 J. Ji, H. Ji, L. Zhang, X. Zhao, X. Bai, X. Fan, F. Zhang and R. S. Ruoff, *Adv. Mater.*, 2013, **25**, 4673.
5 S. Yang, X. Feng, S. Ivanovici and K. Müllen, *Angew. Chem. Int. Ed.*, 2010, **49**, 8408.
6 L. Suo, Y.-S. Hu, H. Li, M. Armand and L. Chen, *Nat. Commun.*, 2013, **4**, 1481.
7 X. Xu, H. Tan, K. Xi, S. Ding, D. Yu, S. Cheng, G. Yang, X. Peng, A. Fakeeh and R. V. Kumar, *Carbon*, 2015, **84**, 491.
8 X. Xu, B. Dong, S. Ding, C. Xiao and D. Yu, *J. Mater. Chem. A*, 2014, **2**, 13069.
9 Y. P. Wu, E. Rahm and R. Holze, *J. Power Sources*, 2003, **114**, 228.

10 X. Zhou, J. Bao, Z. Dai and Y.-G. Guo, *J. Phys. Chem. C*, 2013, **117**, 25367.
11 Z. Zhu, S. Wang, J. Du, Q. Jin, T. Zhang, F. Cheng and J. Chen, *Nano Lett.*, 2014, **14**, 153.
12 M. He, K. Kraychyk, M. Walter and M. V. Kovalenko, *Nano Lett.*, 2014, **14**, 1255.
13 Y. Xu, X. Zhu, X. Zhou, X. Liu Y., Liu, Z. Dai and J. Bao, *J. Phys. Chem. C*, 2014, **118**, 28502.
14 J. Liu, K. Song, C. Zhu, C.-C. Chen, P. A. van Aken, J. Maier and Y. Yu, *ACS Nano*, 2014, **8**, 7051.
15 C. Wang, H. Wu, Z. Chen, M. T. McDowell, Y. Cui and Z. Bao, *Nat. Chem.*, 2013, **5**, 1042.
16 Y. Xu, Y. Zhu and C. Wang, *J. Mater. Chem. A*, 2014, **2**, 9751.
17 J. Chang, X. Huang, G. Zhou, S. Cui, P. B. Hallac, J. Jiang, P. T. Hurley and J. Chen, *Adv. Mater.*, 2014, **26**, 758.
18 X. Zhou, L.-J. Wan and Y.-G. Guo, *Adv. Mater.*, 2013, **25**, 2152.
19 X. Zhou, Y.-X. Yin, L.-J. Wan and Y.-G. Guo, *J. Mater. Chem.*, 2012, **22**, 17456.
20 L. Zhang, H. B. Wu, Y. Yan, X. Wang and X. W. Lou, *Energy Environ. Sci.*, 2014, **7**, 3302.
21 X. Zhou, L.-J. Wan and Y.-G. Guo, *Chem. Commun.*, 2013, **49**, 1838.
22 X. Xu, Z. Fan, X. Yu, S. Ding, D. Yu and X. W. Lou, *Adv. Energy Mater.*, 2014, **4**, 1400902.
23 C. Zhu, X. Mu, P. A. van Aken, Y. Yu and J. Maier, *Angew. Chem. Int. Ed.*, 2014, **53**, 2152.
24 S. Ding, D. Zhang, J. S. Chen and X. W. Lou, *Nanoscale*, 2012, **4**, 95.
25 J. Wang, J. Liu, D. Chao, J. Yan, J. Lin and Z. X. Shen, *Adv. Mater.*, 2014, **26**, 7162.
26 K. Chang and W. Chen, *ACS Nano*, 2011, **5**, 4720.
27 R. Bhandavat, L. David and G. Singh, *J. Phys. Chem. Lett.*, 2012, **3**, 1523.
28 R. Chen, T. Zhao, W. Wu, F. Wu, L. Li, J. Qian, R. Xu, H. Wu, H. M. Albishri, A. S. Al-Bogami, A. A. El-Hady, J. Lu and K. Amine, *Nano Lett.*, 2014, **14**, 5899.
29 J. Liu, Y. Wen, Y. Wang, P. A. van Aken, J. Maier and Y. Yu, *Adv. Mater.*, 2014, **26**, 6025.
30 B. Qu, C. Ma, G. Ji, C. Xu, J. Xu, Y. S. Meng, T. Wang and J. Y. Lee, *Adv. Mater.* 2014, **26**, 3854.
31 H. Wu and Y. Cui, *Nano Today*, 2012, **7**, 414.
32 Y. Xu, Y. Zhu, F. Han, C. Luo and C. Wang, *Adv. Energy Mater.*, 2014, **4**, 1400753.
33 X. Huang, J. Yang, S. Mao, J. Chang, P. B. Hallac, C. R. Fell, B. Metz, J. Jiang, P. T. Hurley and J. Chen, *Adv. Mater.*, 2014, **26**, 4326.
34 N. Liu, Z. Lu, J. Zhao, M. T. McDowell, H.-W. Lee, W. Zhao and Y. Cui, *Nat. Nanotechnol.*, 2014, **9**, 187.
35 X. Zhou, Y.-X. Yin, L.-J. Wan and Y.-G. Guo, *Chem. Commun.*, 2012, **48**, 2198.
36 S. Kong, Z. Jin, H. Liu and Y. Wang, *J. Phys. Chem. C*, 2014, **118**, 25355.
37 Y. Wang, J. Wu, Y. Tang, X. Li, C. Yang, M. Qin, F. Huang, X. Li and X. Zhang, *ACS Appl. Mater. Interfaces*, 2012, **4**, 4246.
38 W. Luo, Y. Xie, C. Wu and F. Zheng, *Nanotechnology*, 2008, **19**, 075602.
39 X. Xia, C. Zhu, J. Luo, Z. Zeng, C. Guan, C. F. Ng, H. Zhang and H. J. Fan, *Small*, 2014, **10**, 766.
40 G. Huang, T. Chen, Z. Wang, K. Chang and W. Chen, *J. Power Sources*, 2013, **235**, 122.
41 F. Zhan, B. Geng and Y. Guo, *Chem.—Eur. J.*, 2009, **15**, 6169.
42 A. N. Grace, R. Ramachandran, M. Vinoba, S. Y. Choi, D. H. Chu, Y. Yoon, S. C. Nam and S. K. Jeong, *Electroanalysis*, **2014**, *26*, 199.
43 Q. Su, J. Xie, J. Zhang, Y. Zhong, G. Du and B. Xu, *ACS Appl. Mater. Interfaces*, 2014, **6**, 3016.
44 Q. Wang, L. Jiao, H. Du, W. Peng, Y. Han, D. Song, Y. Si, Y. Wang and H. Yuan, *J. Mater. Chem.*, 2011, **21**, 327.
45 J. H. Kim, J.-H. Lee and Y. C. Kang, *Electrochim. Acta*, 2014, **137**, 336.
46 J. L. Gomez-Camer, F. Martin, J. Morales and L. Sanchez, *J. Electrochem. Soc.*, 2008, **155**, A189.
47 Y. Gu, Y. Xu and Y. Wang, *ACS Appl. Mater. Interfaces*, 2013, **5**, 801.
48 N. Mahmood, C. Zhang, J. Jiang, F. Liu and Y. Hou, *Chem.—Eur. J.*, 2013, **19**, 5183.
49 Q. Wang, L. Jiao, H. Du, Y. Si, Y. Wang and H. Yuan, *J. Mater. Chem.*, 2012, **22**, 21387.
50 W. S. Hummers and R. E. Offeman, *J. Am. Chem. Soc.*, 1958, **80**, 1339.
51 D. Banerjee, R. V. Jagadeesh, K. Junge, M.-M. Pohl, J. Radnik, A. Brückner and M. Beller, *Angew. Chem. Int. Ed.*, 2014, **53**, 4359.